

KINETIC MODELING OF PARTICLE ACCELERATION IN A SOLAR NULL-POINT RECONNECTION REGION

G. BAUMANN¹, T. HAUGBØLLE^{2,1}, AND Å. NORDLUND^{1,2}

¹Niels Bohr Institute, University of Copenhagen, Juliane Maries Vej 30, DK-2100 Copenhagen, Denmark

²Centre for Star and Planet Formation, Natural History Museum of Denmark, University of Copenhagen, Øster Voldgade 5-7, DK-1350 Copenhagen, Denmark

ACCEPTED TO APJ: *May 13, 2013*

ABSTRACT

The primary focus of this paper is on the particle acceleration mechanism in solar coronal three-dimensional reconnection null-point regions. Starting from a potential field extrapolation of a Solar and Heliospheric Observatory (*SOHO*) magnetogram taken on 2002 November 16, we first performed magnetohydrodynamics (MHD) simulations with horizontal motions observed by *SOHO* applied to the photospheric boundary of the computational box. After a build-up of electric current in the fan-plane of the null-point, a sub-section of the evolved MHD data was used as initial and boundary conditions for a kinetic particle-in-cell model of the plasma. We find that sub-relativistic electron acceleration is mainly driven by a systematic electric field in the current sheet. A non-thermal population of electrons with a power-law distribution in energy forms in the simulated pre-flare phase, featuring a power-law index of about -1.78. This work provides a first step towards bridging the gap between macroscopic scales on the order of hundreds of Mm and kinetic scales on the order of cm in the solar corona, and explains how to achieve such a cross-scale coupling by utilizing either physical modifications or (equivalent) modifications of the constants of nature. With their exceptionally high resolution — up to 135 billion particles and 3.5 billion grid cells of size 17.5 km — these simulations offer a new opportunity to study particle acceleration in solar-like settings.

Subject headings: acceleration of particles magnetic reconnection Sun: fares Sun: corona

1. INTRODUCTION

During solar flares an enormous amount of energy is released, in particular in the form of highly energetic non-thermal electrons. It is generally accepted that the underlying release mechanism is magnetic reconnection. In connection with a reconnecting current sheet, strong large-scale electric fields can build up (Liu et al. 2009) and references therein), leading to direct acceleration of particles beyond thermal velocities, while fluctuating electric fields created by reconnection and other dynamic events can lead to stochastic acceleration (e.g. Miller et al. 1996, 1997; Petrosian et al. 2006).

During the last decade, high-resolution observations of solar magnetic fields from several solar space missions and ground-based observations, such as *YOHKOH*, *SOHO*, *TRACE*, *RHESSI*, *Hinode*, *STEREO*, *Solar Dynamics Observatory* and *Spitzer Space Telescope* (e.g. Longcope et al. 2005; Ko et al. 2003; Milligan et al. 2006; Priest & Schrijver 1999; Sui et al. 2004; Aulanier et al. 2007; Kumar et al. 2012; Jess et al. 2008) have brought new insights regarding the interconnecting and X-ray loops, the current sheet in the reconnection region, upflow velocities of chromospheric evaporation as a result of non-thermal particles impact, and white-light emission during flares and instabilities as possible drivers, providing substantial support for existing solar flare and coronal mass ejection models.

Additionally, new three-dimensional (3D) coronal magnetic reconnection and acceleration models (e.g. Priest & Titov 1996; Vlahos et al. 2004) as well as the rapid expansion of computing resources for large-scale

simulations (Isobe et al. 2007; Galsgaard & Pontin 2011; Toriumi & Yokoyama 2012) have opened up a new chapter in the understanding of the formation of current sheets and particle acceleration sites in 3D reconnection regions. But what is lacking is an interconnected understanding of how microscopic plasma physics scales interact and exchange information with macroscopic large-scale magnetohydrodynamics (MHD) scales in the solar atmosphere. MHD scales provide the environment for particle acceleration to happen, but it is unclear how the complex non-linear feedback from much smaller scales onto the overall behavior of the plasma above the solar surface is handled by nature.

Most studies have made use of the fact that the temporal evolution of the large-scale magnetic field in the solar atmosphere can to a first approximation be described by compressible MHD. But fluid approaches are limited to thermal particle distributions, which is not sufficient to describe the kinetic aspects of magnetic reconnection that convert magnetic field energy into particle kinetic energy. A proper description of such processes requires taking into account the back-reaction of kinetic processes on the large-scale dynamics. Nevertheless, test particle MHD simulations, (e.g. Turkmani et al. 2005, 2006; Browning et al. 2010; Dalla & Browning 2005, 2008; Rosdahl & Galsgaard 2010), give a good idea of the overall acceleration region framework. In such simulations, MHD fields evolve independently of the motion of the test particles. There is no immediate back-reaction from the accelerated particles onto the fields, which is potentially a serious limitation, since especially the changes of the electric field that would be induced by the accelerated particles can be large compared to the background field

induced by magnetic reconnection (Siversky & Zharkova 2009). The lack of feedback can lead to an exaggerated particle acceleration, as has been noted by, for example, Rosdahl & Galsgaard (2010), since there is no limitation for the energy gain of particles. Furthermore, kinetic instabilities can be of importance for the fast reconnection onset in solar flares, and more generally for the evolution of the current sheets in reconnection regions (Bárta et al. 2010). There is therefore a need for realistic self-consistent kinetic simulations to examine micro-scale processes in plasmas and to be able to properly take into account back-reactions from the particles to the fields.

The main challenge for kinetic simulations on scales of solar events is the enormous dynamic range involved. Explicit particle-in-cell (PIC) simulations have to resolve characteristic kinetic scales and are restricted to very small physical sizes, due to limitations that arise from conditions for code stability as well as from resolution criteria. These computational restrictions have so far prevented investigations of the coupling of kinetic to MHD scales using kinetic simulations, and have thus prevented self-consistent modeling of particle acceleration in solar flares. There has mainly been one interlocked model attempt by Sugiyama & Kusano (2007), who ran PIC simulations embedded in a large-scale MHD simulation with PIC boundary conditions defined by the surrounding MHD domain. The particle information was similarly passed from the MHD to the kinetic simulation areas as it is done in the present study. But the complexity of the problem especially in the transition zone between MHD and PIC zones combined with the simultaneity of the two simulations limits the applicability of such attempts significantly. In the present study, we introduce a new method to meet the challenge of multi-hierarchy simulations and use the method to investigate particle acceleration mechanisms in a solar reconnection pre-flare event using ultra-large-scale kinetic modeling. We further discuss the limitations of this new way to combine macroscopic and microscopic scales.

In Section 2, we describe the numerical methods and their implementation, while in Section 3 we introduce the experimental setup and the necessary modifications and list the most important simulations we performed, indicating their relative roles and importance. In Section 4, we present and discuss the results including a comparison to observational studies. Finally, in Section 5, we summarize the results, present our conclusions, and give an outlook onto future work.

2. METHODS

We perform PIC simulations using the *Photon-Plasma* code (Haugbølle 2005; Hededal 2005), which solves the Maxwell equations

$$-\frac{\partial \mathbf{B}}{\partial t} = \nabla \times \mathbf{E} \quad (1)$$

$$\epsilon_0 \mu_0 \frac{\partial \mathbf{E}}{\partial t} = \nabla \times \mathbf{B} - \mu_0 \mathbf{J}, \quad (2)$$

together with the relativistic equation of motion for charged particles

$$m \frac{d(\gamma \mathbf{v})}{dt} = q(\mathbf{E} + \mathbf{v} \times \mathbf{B}) \quad (3)$$

on a staggered Yee lattice (Yee 1966). We use SI units, scaled so the unit of length is 1 km, the unit of time is 0.1 s, and the unit of density is $10^{-12} \text{ kg m}^{-3}$.

The Lorentz force is computed by interpolation of the electromagnetic fields \mathbf{E} and \mathbf{B} from the mesh to the particle positions, employing a cubic scheme using the 64 nearest mesh points. The code integrates the trajectories of protons and electrons moving in the electromagnetic field with a Vay particle mover (Vay 2008). The charge density ρ is determined by weighted averaging of the particles to the mesh points using the same cubic scheme as for the field to particle interpolation, to avoid self forces. The currents are found using a new 6th order version of the Esirkepov charge conservation method (Esirkepov 2001) that is consistent with the field solver¹. The field equations are solved on the mesh using an implicit 2nd order in time and 6th order in space method. Because the solver is charge conserving and the fields are properly staggered, Gauss' law is obeyed and the \mathbf{B} field is kept divergence free to numerical precision.

The boundaries of the domain are fixed for the magnetic fields and open for particles. Particles can escape and new particles are added to the box from 'ghost cells' outside the physical boundaries, where the conditions are specified from values in the MHD snapshot. In the current short-duration kinetic simulations, the field values in the boundaries are held fixed. In longer duration simulations, they could be made time dependent by performing interpolations in time between MHD snapshots. See also Haugboelle et al. (2012).

Below we introduce for the first time a modification of the elementary charge q , in addition to and analogous to the well-known speed of light (c) modification that has previously been used in many cases (e.g. Drake et al. 2006). Since all the micro-scales (gyro-radii, skin depths, Debye lengths) are inversely proportional to the charge per particle, one can increase the micro-scales until they are resolvable on macroscopic scales by decreasing the charge per particle sufficiently.

While changing the ratio of micro- to macro-scales by a large amount may appear to be a very drastic approach, the method can be defended on both qualitative and quantitative grounds: from a qualitative point of view, it may be argued that as long as one retains a proper ordering of non-dimensional parameters, as discussed in more detail below, one should expect to see essentially the same qualitative behavior, albeit with (possibly large) differences in quantitative aspects. From a quantitative point of view, one can indeed attempt to predict how these quantitative aspects depend on the modifications of q and c , to be able to extrapolate—at least to order of magnitude—to values that would be typical in the unmodified system.

Adopting this approach enables us to perform explicit PIC simulations of large-scale plasmas. With the parameter values used here we resolve the electron skin depth $\delta_{skin,e}$ with at least 3.8 grid cells and the Debye length with at least 0.3 grid cells. For the time stepping, we use a Courant condition of 0.4, considering the light crossing time in a grid cell as well as the local plasma frequency.

¹ The original Esirkepov method, just like most other charge conserving schemes in the literature, is only consistent with a 2nd order field solver.

3. SIMULATIONS

In order to investigate the particle acceleration mechanism around a 3D reconnection region, we started out with a Fourier transform potential extrapolation of a *SOHO*/Michelson Doppler Imager magnetogram from 2002 November 16 at 06:27:00 UT, 8 hour prior to a C-flare occurrence in the AR10191 active region. This is similar to the setup by Masson et al. (2009). As there is no vector magnetogram available for this event, a non-linear force-free extrapolation has not been feasible. The potential field magnetic configuration arising from the extrapolation showed mainly two connectivity regions, separated by a dome-shaped ‘fan-surface’ (Craig et al. 1997), each including a spine structure, which is the symmetry line intersecting the fan at the magnetic null-point. Although initially strove for, the given setup did not lead to a flare-like plasma eruption. The MHD simulation hence describes a pre-flare phase with a characteristic 3D magnetic reconnection region.

We define the inner spine as the spine intersecting with the solar surface inside the dome-like surface delimited by the fan-plane, while the outer spine reaches up into the corona before returning to the photosphere several tens of Mm away from the null-point (cf. Figure 1). The magnetic field lines in the fan-plane meet at the magnetic null-point, which is located at about 4 Mm above the photospheric boundary.² The dome-like fan-plane is a typical feature of a parasitic polarity magnetic null-point topology originating when a vertical dipole field emerges into a magnetic field configuration of opposite magnetic polarity. For an elaborated description of the observations of this solar flare event, see Masson et al. (2009).

The MHD simulations of this event previously conducted using the fully 3D resistive compressible *Stagger* MHD code (Nordlund & Galsgaard 1997) on a box size of $175 \times 100 \times 62$ Mm and a stretched $896 \times 512 \times 320$ grid with a minimum cell size of ≈ 80 km in a region around the null-point (Baumann et al. 2013) establishes the initial condition for the PIC simulations. In most cases, the initial MHD particle density and temperature were set to the constant values of $6.8 \times 10^{12} \text{ cm}^{-3}$ and 5×10^5 K, neglecting gravity, analogously to Masson et al. (2009). The boundaries were chosen to be closed at the bottom and top, and periodic on the sides. Assuming, as did Masson et al. (2009), that the strong horizontal motions observed by *SOHO* during the considered time interval was the driver of the reconnection event, we simulated the plasma motion caused by these motions by using essentially the same elliptically shaped driver at the photospheric boundary of the box as was used by Masson et al. (2009), applying velocity amplitudes ranging from 3.33 to 20 km s^{-1} and a horizontal shape function schematically representing the observed photospheric motion. The enhanced driving speed, compared to observations, led to a significant reduction of the simulation time, while it was still sub-Alfvénic and thus left the overlying plasma and magnetic field enough time to adapt to the displacement.

The line-tied photospheric boundary motions indi-

rectly reshuffled the fan-spine geometry at its foot-points by a pressure increase onto the fan-plane, which caused a relative displacement of the magnetic field lines inside and outside the fan-plane of the magnetic null-point, respectively, resulting in the formation of a current sheet in the fan-plane. The displacement of field lines also causes a relative displacement of the two spines, which then leads to magnetic reconnection at the null-point and a growing resistive electric field in the fan-plane. A detailed description of the MHD simulations and their results are published in a companion paper (Baumann et al. 2013).

For the present study, we used an MHD simulation with an initial particle density of $6.8 \times 10^{12} \text{ cm}^{-3}$, a temperature of 5×10^5 K, and an applied driving speed of 20 km s^{-1} . After 240 seconds of simulated solar time, the null-point area showed clearly enhanced current densities parallel to the magnetic field, indicating that a dissipative process was taking place. We choose this as the starting point for the 3D relativistic PIC simulation. To minimize computational constraints due to the plasma frequency, we rescale the density from the essentially chromospheric value of $6.8 \times 10^{12} \text{ cm}^{-3}$ used by Masson et al. (2009) partway toward values more characteristic of an active region corona, so that it becomes instead $1.28 \times 10^{11} \text{ cm}^{-3}$.

Figures 1(a) and (b) illustrate the initial PIC simulation setup, by showing the chosen cut-out of a snapshot from the MHD simulation, as seen along the x and y axis respectively. The outer spine extends to the right of Figure 1(b), while the fan-surface spreads out over the rest of the area. Due to the initial difference in the fan-plane eigenvalues (Masson et al. 2009), a slight asymmetry in the fan-surface is noticeable. The inner spine can be recognized inside the volume spanned by the fan-plane field lines in Figure 1(a).

For the kinetic simulations, we use the *Photon-Plasma* code on a uniform grid. A cut-out of the MHD simulation box with dimensions $44 \times 25 \times 16$ Mm is chosen for a set of simulations, covering cell sizes from 70 km down to 17.5 km corresponding to uniform grids with up to $2518 \times 1438 \times 923$ cells. The simulations are generally performed with 20 particles per species per cell, covering up to 30 solar seconds. We neglect gravitation, since the aim of this study is mainly to assess the electron acceleration mechanism, for which the influence of the gravitational force is negligible. The initial ion velocities consist of two components; a random thermal velocity drawn from a Maxwellian distribution plus the bulk velocity from the MHD simulation. For the electron velocities, we use the sum of a random thermal velocity drawn from a Maxwellian distribution, the bulk velocity, and the velocity due to the initial electric current. The initial electric field is simply taken as the advective electric field ($-\mathbf{u} \times \mathbf{B}$, where \mathbf{u} is the MHD bulk velocity) from the MHD simulation, which will be self-corrected by the system after the first few time-steps of the kinetic simulation, by adapting the electric field as well as the electric current to balance the system.

3.1. Modifications to Resolve Kinetic Scales

It is common in MHD and PIC simulations to convert physical units into numerically more convenient code units. Such a rescaling leaves the simulated physical situ-

² For computational reasons, we tapered off the vertical magnetic field toward the boundaries of our horizontally periodic MHD model, and the height of the null-point is therefore different from the case in Masson et al. (2009).

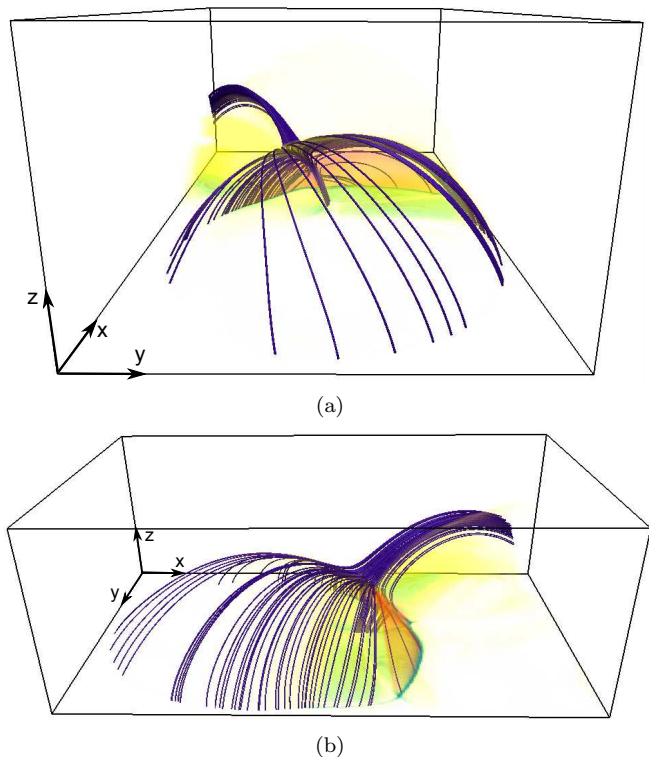


FIG. 1.— Initial state of the PIC code simulation; a cut-out of size $44 \times 25 \times 16$ Mm of an evolved MHD simulation snapshot. (a) Seen along the x -axis and (b) along the y -axis. Shown are magnetic field lines (purple), the maximum current density at the lower boundary (turquoise), and the electric current density as a semitransparent direct volume rendering (yellow for lowest value, and orange for highest value).

ation completely unaffected and all parameters can easily be rescaled back to physical units at any time. Because they leave the ratio of scales unaffected these kinds of conversions between units of measurement are not sufficient to allow explicit PIC codes to address the multi-scale issues discussed below.

Magnetic reconnection is a typical example of multi-scale physics, where microscopic scales interact with and couple to macroscopic scales. While kinetic scales in the solar corona are on the order of mm, coronal structures such as the ones investigated here have scales on the order of tens of Mm. This range of spatial scales is impossible to cover by explicit kinetic simulations — now as well as in the foreseeable future. Explicit PIC codes are subject to a number of numerical stability constraints. For the code that we use here, one of them is that the Debye length, defined as $\lambda_D = \sqrt{\epsilon_0 k_B T / n_e q_e^2}$, where k_B is the Boltzmann constant, T the temperature, ϵ_0 the vacuum permittivity, n_e the electron density, and q_e the electron charge, should be at least on the order of a fraction of a grid cell Δs :

$$0.3 \Delta s \lesssim \lambda_D. \quad (4)$$

In addition, there are also stability constraints on the time step set by the speed of light and the plasma frequency

$$\Delta t < \Delta s / c, \quad (5)$$

$$\Delta t \lesssim 2 / \omega_p. \quad (6)$$

In summary, code stability requires that the time step needs to approximately resolve the light-wave and plasma-wave propagation and that the grid spacing should not severely under-resolve the electron Debye length. When these conditions are marginally fulfilled in the global simulation domain, they are typically (except for the speed of light condition) fulfilled with a good margin in most computational cells, which helps to improve the accuracy of the numerical solution.

Additionally, we need to fulfill the following approximate equality:

$$\delta_{skin} \approx \text{a few} \cdot \Delta s. \quad (7)$$

This requirement arises to ensure a reasonably faithful representation of the plasma, as employing too few grid cells per skin depth suppresses sub-skin depth plasma behavior, while, for a fixed number of grid cells, having too many grid cells per skin depth results in a model where the kinetic scales and the MHD scale are not sufficiently separated, and consequently, the MHD behavior is lost. Given these constraints, we would require approximately one septillion (1×10^{24}) grid cells for an unmodified simulation to simultaneously resolve the microscopic and macroscopic scales in the problem. This fundamental constraint notwithstanding, bridging the large-scale difference is in fact approachable. One can either change some of the physical properties (e.g. the magnetic field strength or the plasma density) or, equivalently, modify some of the constants of nature. As long as such modifications of the physical properties of the system do not change the large-scale behavior, they may be helpful by decreasing the gap between microscopic and macroscopic scales.

We first introduce two possible sets of modifications of the physical properties which conduce to decrease the large gap between the micro-scales and the macro-scales, using three modification parameters, which are closely related to each other, so that only two of them are so to speak free parameters, while the third one is a result thereof. One of the reasons for this is an MHD variable constraint; we wish to maintain the relative importance of magnetic and fluid pressure, i.e., we wish to keep the plasma beta parameter unchanged in each type of modification. The goal is to change micro-scales, which cause the previously mentioned numerical constraints, Equations (4)–(7), i.e. increasing the Debye length λ_D , decreasing the span of velocities (equivalent to decreasing the speed of light), and decreasing the plasma frequency. In modification of type A we change the magnetic field strength by a factor $b < 1$, implying a change in the density to keep the pressure balance. This increases the length scales (λ_D , the gyro-radius r_g and the skin depth δ_{skin}) and at the same time reduces the frequencies (ω_p and the gyro-frequency ω_g) by the same factor, while leaving the temperature and hence the sound speed v_s and Alfvén speed v_A of the system unchanged.

Modifications of type B address the macroscopic speed ratios. We start by changing the temperature by a factor t^2 , which then leads to an increase in the acceleration of gravity g by the same factor, as the scale height is proportional to T/g . The consequences of this modification are that speeds increase by a factor t , while the length and frequency ratios are forced to be changed to achieve these required modifications, which means that for this

type of change one cannot maintain the micro-scale ratios.

These modifications of physical properties are equivalent to changing the constants of nature q and c ; the unit of charge and the speed of light. Then q^{-1} determines the ratio between micro and macro-scales through the charge density and c^{-1} influences the ratio of the speeds. μ_0 needs to be kept constant, in order to keep the magnetic pressure and hence the plasma beta unchanged, hence ϵ_0 is the parameter that needs to be modified. Here is a summary of these two types of modifications:

A: PHYSICAL CHANGES: $B \sim b, \rho \sim b^2, T = \text{constant}$

CONSEQUENCES: $\lambda_D \sim \delta_{skin} \sim r_g \sim b^{-1}, \omega_p \sim \omega_g \sim b, v_A \sim v_s \sim v_{th} = \text{constant}$

B: PHYSICAL CHANGES: $T \sim t^2, g \sim t^2, B \sim t, \rho = \text{constant}$

CONSEQUENCES: $\lambda_D \sim t$, but $\delta_{skin} \sim \omega_p = \text{constant}, v_A \sim v_s \sim v_{th} \sim t$.

The idea of modifying the constants of nature has previously been employed. Drake et al. (2006) reduced in their approach the speed of light c , while Siversky & Zharkova (2009) reduced the particle density, which has the same effect on the micro-scales as lowering the charge per particle. In fact, one can show that changes of on the one hand temperature and particle density, and on the other hand changes of the speed of light and the charge per particle, have similar effects: decreasing the speed of light or increasing the temperature (squared) both reduce the ratio of the speed of light to the thermal speed, and decreasing the particle density or the charge per particle both increase the ratio of micro- to macro-scales (adjusting at the same time the magnetic field so as to keep the plasma beta the same). So, in that sense, our changes of the speed of light and the electric charge per particle effectively corresponds to simulating a coronal region with a very high temperature and a very low particle density.

Apart from the modifications discussed above, a reduction of the ratio of the electron to proton mass from 1836 to 18 is used. This is done to decrease the gap between the ion and electron plasma frequency and skin depths to acceptable values. It is a standard trick in PIC simulations, and mass ratios above 16 are normally considered enough to separate the two scales.

Decreasing the ratio between the different speeds (e.g. by lowering the speed of light) are generally motivated by an assumption that if the speeds are nevertheless much smaller than the speed of light, one expects only very marginal changes in the dynamics, while the savings in computing time (which scales as the speed of light) are considerable.

Changing the charge per particle with a large amount (on the order of 10^6 here) is more drastic, but is necessary to bring micro-scales into a realm that is resolvable with current computing resources. To lowest order, such a change of scales is not expected to change the magnetically dominated dynamics dramatically; charged particles are still forced to move essentially along magnetic field lines, with gyration orbits oriented in essentially the same manner with respect to the large-scale structures. What changes is exactly what is required

to change, namely, the ratios between micro- and macro-scales. Any effect that depends on this ratio then changes in an in principle predictable fashion, and one can, a posteriori, attempt to compensate for this, when analyzing and discussing the results, as is done below in Section 4.2.

A crucial point when modifying the constants of nature is to ensure that the hierarchy of characteristic speeds, times, and length scales are, to the largest extent possible, kept as in the real average coronal environment. For the characteristic speeds, this hierarchy is

$$v_d < v_{th,p} \sim v_s < v_{th,e} < v_A < c, \quad (8)$$

where v_d is the average electron drift speed that arises due to the electric current, $v_{th,p(e)}$ is the thermal speed of protons(electrons), v_s is the speed of sound, v_A is the Alfvén speed, and c is the speed of light. For the corona, the values of these inequalities can be approximated by the following numbers (km s^{-1}):

$$0.002 < 90 < 3\,900 < 12\,000 < 300\,000. \quad (9)$$

In contrast to MHD simulations of a solar event, the magnitude of the parameters of a scaled PIC simulation cannot be directly compared to observationally obtained values, since the modifications of the constants of nature have an influence on the magnitudes of the parameters. But estimating what the corresponding solar values would be is possible, by careful rescaling.

We measure all quantities in scaled SI units (unit of length = 1 km, unit of time = 0.1 s, and unit of mass density = $10^{-12} \text{ kg m}^{-3}$).

3.2. Modification Validation

To analyze the influence of the presented modifications onto the physical processes at work, we performed several simulation runs with different physical resolutions and modifications of q and c . A subset of the relevant simulations may be found in Table 1 which summarizes the typical initial run parameters for each simulation.

Run 1S is the smallest run, which therefore corresponds to the size category S , while category M runs have double the physical resolution and L simulations correspondingly a four times higher physical resolution. Runs 1S, 3M and 5L have a constant ratio of the cell size per kinetic scale and hence test the numerical convergence of the simulation results. Run 5L is of special interest, due to its drift speed that is lower than the thermal electron speed, as is the case in the real Sun. Furthermore, a comparison of runs 3M and 2M shows the effects of a change of the micro-scales while keeping the resolution constant. These two case comparisons are especially interesting when considering the kinetic energy distribution for high-energetic particles as, e.g. power-law indices can be validated against observations. In both cases, as presented in Section 4.5, the distributions are, despite their differences in the modification of the constants of nature, very similar and, as mentioned in Section 5, their power-law indices are comparable to observational results. This indicates, that the influence of the chosen numerical resolutions onto the physical acceleration process of particles in the reconnection region is small. Run 4M is specifically interesting when looking at the upper energy limit of the kinetic energy distribution of particles, as it shows the influence of an increase in the speed

of light onto the energy gain of particles. Very little difference in the energy distribution could be found, which attests the reduction of the speed of light as a reasonable modification as long as one conforms to the speed hierarchy. We also increased the systems temperature by a factor of two for run 2M and run 3M resulting in run $2M_T$ and run $3M_T$. This increase in temperature causes the high-energy tail to (partially) drown in the thermal particle energy distribution, so that a study of the nature of non-thermal particle acceleration in the chosen magnetic field geometry is no longer possible as no clear distinction between the two energy ranges can be made.

The results of these modification studies are in more detail reported in Section 4.5. Section 4.2 additionally discusses the resulting electric fields of most simulation runs, listed in Table 1. In summary, we note that except for the under-resolved run 1S, the electric fields of simulations with different modifications cover a rather small range of values.

4. RESULTS AND DISCUSSION

There are several objectives with these experiments, but the most important one is to establish whether any particle acceleration (i.e., production of non-thermal particles) takes place in the experiments and if so, what the main particle acceleration mechanism at work is. As we demonstrate and discuss below, non-thermal particles are indeed being produced. Their energy distributions are approximate power laws, with slopes similar to the slopes inferred from observations of the bulk of sub-relativistic accelerated electrons in magnetic reconnection events in the solar corona.

Most importantly, the presented simulations manifest the main electron accelerator as being a systematic electric field, which evolves relatively slowly, and which we therefore characterize as being essentially a ‘direct current’ (DC) electric field. This does not mean that the field is completely stationary, nor that time evolution is unimportant. What it does mean is that we can demonstrate that power-law distributions of electrons can be created even by nearly stationary electric fields, as a result of basically geometric factors, and without reliance on a recursive process in time. Such systematic electric fields occur in our experiments in connection with the strong current sheets that build up as a consequence of the imposed stress on the magnetic field.

In the beginning of the PIC simulations we generally observe a strong increase in the electric current density and the electric field in the fan-plane, close to the location where the relative inclinations between the magnetic field lines of the two conductivity domains—the inner and outer fan-plane area—are largest, but also close to the inner spine. Due to the boundary conditions chosen, we see a motion of the inner spine as well as a relative motion between the inner and outer spines, where their relative distance increases with increasing stress and decreases as the system relaxes, as discussed also in the corresponding MHD simulation article Baumann et al. (2013). The photospheric boundary motion triggers magnetic reconnection at the null-point by adding shear between the inner and the outer magnetic field lines of the fan-surface, which causes stress on the system that can only be reduced by dissipative processes, including magnetic reconnection. The resulting

current sheet after 8 seconds of solar time in simulation run 3M is shown in Figure 2, which also shows the location of the non-thermal high energetic electrons (arrows), located in the current sheet of the fan-plane outlined by magnetic field lines, coinciding with the location of an enhanced electric field and $E \parallel \hat{B}$. The semitransparent light blue surface depicts the highest electric current density, which is located in the fan-plane. A fraction of the high-energetic electrons move through the null-point up along the outer spine. Due to the increasing magnetic field strength with increasing distance from the null, these particles will essentially follow the magnetic field lines, and will, unless reflected by a magnetic mirroring effect, likely impact the solar surface where the strongly bent outer spine intersects with the photosphere. The other (larger) fraction of non-thermal particles passes the null-point and impacts the photosphere on the north-west side of the fan-plane (to the left in Figure 2). A comparison of this impact region with the observations of this event reveals several similarities, as discussed in Section 4.4. The electrons in the fan-plane experiences a strong acceleration parallel to the magnetic field inside the current sheet while approaching the null-point.

4.1. The Occurrence of Electric Fields in MHD and PIC Experiments

A systematic electric current develops in the fan-plane as a result of the photospheric driver, which introduces a near discontinuity in direction of the magnetic field in the two regions with different connectivity; outside and inside the fan-plane. This occurs already in the MHD experiment, where the electric current \mathbf{J} is identically equal to $\nabla \times \mathbf{B}$ (disregarding constant factors), and where the corresponding electric field in the local reference frame, here called the *diffusive electric field*, is given by an Ohm’s law of the type $\mathbf{E}_\eta = \eta \mathbf{J}$, where η is a numerical resistivity.

Apart from rapid fluctuations (on plasma frequency time scales) a similar equality between $\nabla \times \mathbf{B}$ and the electric current \mathbf{J} must also hold in the PIC experiment. Because the PIC simulations are collisionless one would perhaps expect that the diffusive part of the electric field, initially not inherited from the MHD simulation (only the advective, $-\mathbf{u} \times \mathbf{B}$, part is kept in the PIC initial condition), would remain negligibly small. The results of our experiment shows, however, that this is not the case. Instead of remaining small, the diffusive electric field actually grows in magnitude, although it generally remains much lower (after taken into account the modifications as per Section 4.2) than in the MHD simulation from which the PIC simulations were started.

On closer inspection, the reason for the growth of the electric field becomes obvious: the charged particles that carry the electric current — this is primarily the electrons — cannot go wherever they want by following the slightest whim of a tiny electric field (in the frame of reference moving with the current). Instead, they are in general forced to follow magnetic field lines. But even along field lines, the charged particle motions are not unhindered; already modest (local or global) increases of the magnetic field can force a charged particle to become reflected. In addition, systematic or fluctuating cross-field components of the electric field may cause charged

TABLE 1
SUMMARY OF SIMULATION RUNS.

Run	Δs (km)	$\delta_e/\Delta s$	Δt	$r_g/\Delta s$	$\lambda_D/\Delta s$	c (km s $^{-1}$)	v_J (km s $^{-1}$)	No. of Cells	No. of Part.	t (s)
1S	70	5	0.0072	0.24	0.4	3900	28	54 M	2.1 B	21
2M	35	10	0.0036	0.48	0.8	3900	28	427 M	17 B	17
3M	35	5	0.0036	0.2	0.4	3900	32	427 M	17 B	30
4M	35	5	0.0013	0.2	0.2	7800	32	427 M	17 B	17
5L	17.5	5	0.0018	0.1	0.4	3900	22	3.4 B	136 B	12
3M _T	35	5.5	0.0036	0.77	1.3	3900	63	427 M	17 B	12
2M _T	35	11	0.0036	1.55	2.6	3900	67	427 M	17 B	12

Notes. Given are median values over the entire domain for all the ratios of parameter per cell size Δs . $\delta_e = c/\omega_{pe}$ is the skin depth, where c is the speed of light, ω_{pe} is the plasma frequency, Δt the time step, $r_g \approx v_{th,e}/\omega_{ce}$ the gyro radius, where ω_{ce} is the electron gyro-frequency, $\lambda_D = v_{th}/\omega_{pe}$ is the Debye length and $v_J = J/(qn)$ is the electron current velocity. Further listed are the number of cells and particles used for each simulation and the simulated time t in solar seconds. The runs with the attribute T have twice the temperature compared to the other simulations runs.

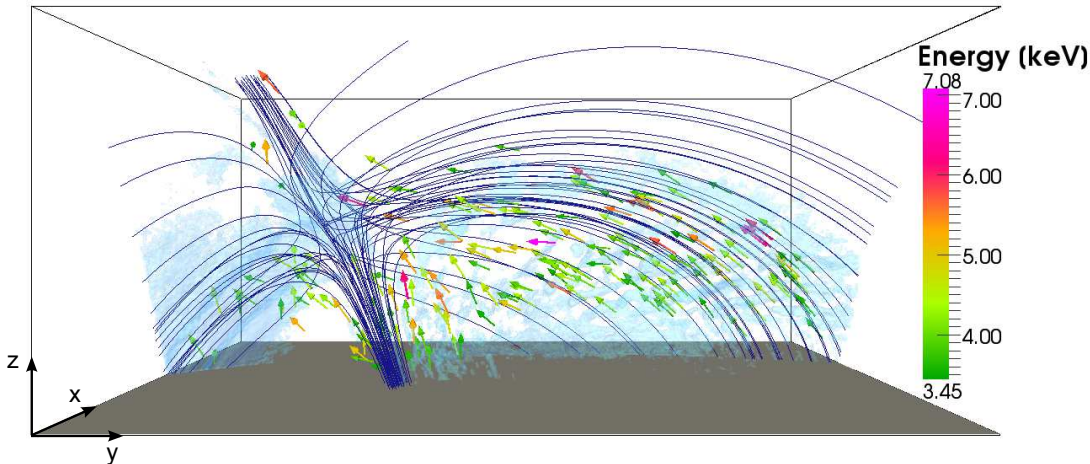


FIG. 2.— Random selection of non-thermal electrons (arrows with color indicating their energy) in the current sheet (semitransparent light blue), which is located in the fan-plane, together with the magnetic field (dark blue) for run 3M. The spine of the topological structure stretches into the left upper corner (outer spine) and reaches down into the center of the dome-shaped fan-plane (inner spine).

particles to drift away from its initial field line, especially in low magnetic field strength regions, and in regions with significant shear of magnetic field lines; i.e., precisely in regions with significant net electric currents.

In particular, it is clear from the very definition of the concept that magnetic reconnection causes a continuously on-going change of magnetic connectivity, and that this change occurs exactly in the place where the largest electric current needs to be maintained.

The component of the electric field along B , $E\|\hat{B}$, corresponds closely to the diffusive electric field in MHD when considering the corona. $E\|\hat{B}$ is plotted together with the magnitude of E in $V\ m^{-1}$ for runs 1S, 2M, 3M, 5L, 2M_T, and 3M_T in Figure 3. In the snapshot from the MHD run used for the PIC simulations, we find diffusive electric field values of about $29\ V\ m^{-1}$ and a total electric field of $1666\ V\ m^{-1}$. A comparison of the locations of high diffusive electric fields in the MHD with regions of high $E\|\hat{B}$ in the PIC simulations show that the peak values can be found in both cases in the current sheet, while when comparing the advective electric fields, it reveals that, unlike in MHD case, the PIC advective electric fields peak again in the current sheet. In the MHD case, this quantity is high in most of the domain around the null-point, while in the PIC case it is only high in-

side the current sheet. Both differences (magnitude and peak location of the advective electric field) are presumably a consequence of lowering the elementary charge, imposed by the modifications. The lower the charge, the higher the speeds of the (lightest) particles have to be in order to maintain the same electric current, set by the magnetic field geometry. Therefore, the diffusive as well as the advective electric field adapt to higher values in the PIC simulations, particularly in the current sheet. As previously mentioned, our modifications of the constants of nature prevent us from directly comparing these electric field values to the values obtained in the MHD simulations. But, as shown in the next section, we are able to make a qualified guess as to what the PIC electric fields would be in the real solar case, which we further compare to the MHD electric fields. While most medium-resolution runs (cf. Table 1) show comparable electric fields (Figure 3), with differences of a factor of 2–3, run 1S is under-resolved, and clearly disagrees with all other simulation runs.

Charged particles moving in a realistic (non-smooth) electro-magnetic field effectively experience a ‘resistance’, and a non-negligible, systematic electric field is needed to maintain the electric current \mathbf{J} consistent with $\nabla \times \mathbf{B}$, as required by the Maxwell equations. Below we demonstrate that, at least in our numerical experiment,

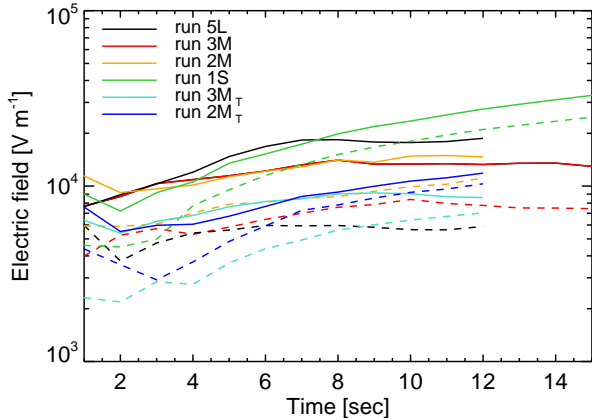


FIG. 3.— Average magnitude of the largest total electric field (solid) and $E\|B$ (dashed) calculated on a cut-out around the null-point with dimensions $13 \times 21 \times 16$ Mm over the number of grid points covering 1 Mm for runs 2M, 3M, and 5L and the higher temperature runs $2M_T$ and $3M_T$.

it is this systematic electric field that is mainly responsible for the particle acceleration. We then argue that, since the same phenomena must occur in the real solar case, a similar particle acceleration mechanism must be at work there.

4.2. The DC Electric Field as the Particle Accelerator

The systematic electric field which develops across the fan-plane peaks where the electric current density is largest. This is where particles are mainly being accelerated and where the major contribution to the power-law energy distribution population presented in Section 4.5 comes from. Its origin is the tendency for an imbalance between the current density and the curl of the magnetic field, which occurs as a consequence of the dissipative reconnection processes. As magnetic field lines are reconnected, the charged particles that flow along them become ‘misdirected’ and need to be replaced by the acceleration of new particles that are now, instead of the previous ones, situated correctly with respect to the magnetic field and its curl.

Tracing particles with kinetic energies in the high-energy tail and interpolating the fields to the particle position in time-steps of 0.003 seconds for 5 solar seconds in run 3M, the direct correlation between a continuous energy gain for electrons and a negative electric field component in the direction of motion is apparent. These non-thermal particles are primarily found in regions close to, or inside, the current sheet of the fan-plane, where the electric current density is highest. In Figure 4, seven representative non-thermal particles that gain energy during approximately 4 solar seconds are shown using different colors. Plotted to the left are their energy, the electric field component pointing in the direction of the particle velocity $E\|v$, the cosine of the pitch angle $\cos(B, v)$, and the gyro-radius r_g . An indication of the particle speeds may be obtained by observing the paling of the line color in their trajectories to the right which are superposed on the images of the sum over electric current density slices. The upper panel shows the sum of xy -slices from a height of 2.5–2.9 Mm illustrated in (a) (see top of figure), while the lower panel displays xz -slices av-

eraged over 12.6–13.4 Mm in the y -direction as shown in (b) of Figure 4. Both background images are taken at time $t = 6$ seconds and raised to the power 0.5 to enhance the visibility of the fine structures. It is essential to mention that these images only change slightly during the presented time interval. The null-point is located at [26.5, 13.9, 2.8] Mm, illustrated by a cross-hair. Note, the particle trajectories are marginally displaced, due to their projection onto the current density planes.

Similar plots, but for particles that lose energy, are shown in Figure 5. Electrons starting from the right-hand side of the current sheet feel first a very diffuse and rapidly changing electric field, due to a fragmentation of the current sheet, which first develops there. This behavior is most evident when looking at the green energy bump around time 5 seconds in the first panel of Figure 4. In such fluctuating regions, there is a constant competition between the dominance of the perpendicular electron movement in-between the strong $E\|B$ patches and the parallel motion inside an $E\|B$ region. But once a particle is inside a current filament the velocity is mostly directed oppositely to the electric field, and electrons then experience a rapid acceleration, due to which the perpendicular energy relative to the magnetic field becomes negligible and the electrons move almost parallel to the magnetic field (cf. the $\cos(\text{pitch angles})$ in Figure 4 and 5). The gyro-radius is permanently very small (on the order of 3 – 8 km), meaning that electrons tightly follow the magnetic field lines. When particles approach the null-point (marked by the cross-hair in the graphics), their gyro radius naturally grows, as $r_g \propto v_{\perp} \cdot B^{-1}$. At the same time, the magnetic field is weak enough that the electrons are no longer strongly confined to the magnetic field lines, and they are instead directly accelerated by the electric field, rather independent of their orientation relative to the magnetic field. Particles entering the region close to the strongest current sheet may also experience a modest growth in gyro-radius, as the magnetic field there is rather weak.

Small-scale regular oscillations which can especially be seen in the $E\|v$ and in the $\cos(\text{pitch angle})$ in the panels of Figures 4 and 5 occur at a frequency of about 7.65 s^{-1} , which is of the order of the plasma frequency.

We provide in Figure 3 as well as in Figures 4 and 5 electric field values which are affected by our modifications of the constants of nature. We therefore need to address how to transform these values back, in order to make them comparable to the MHD simulation results as well as to observations.

For this purpose we start out with the force that an electron with charge q and mass m_e experiences when moving in an electric field E , assuming that the DC electric field is the main particle accelerator $F = qE = m_e a$. We further neglect the displacement current since the accelerating electric field—ignoring small-scale turbulence—is persistent. At time t and after having covered a distance $L = \frac{1}{2} a t^2$ the electron has a velocity v of

$$v = a t = (2La)^{1/2} = \left(\frac{2LqE}{m_e} \right)^{1/2}. \quad (10)$$

The electric current has to balance the magnetic field

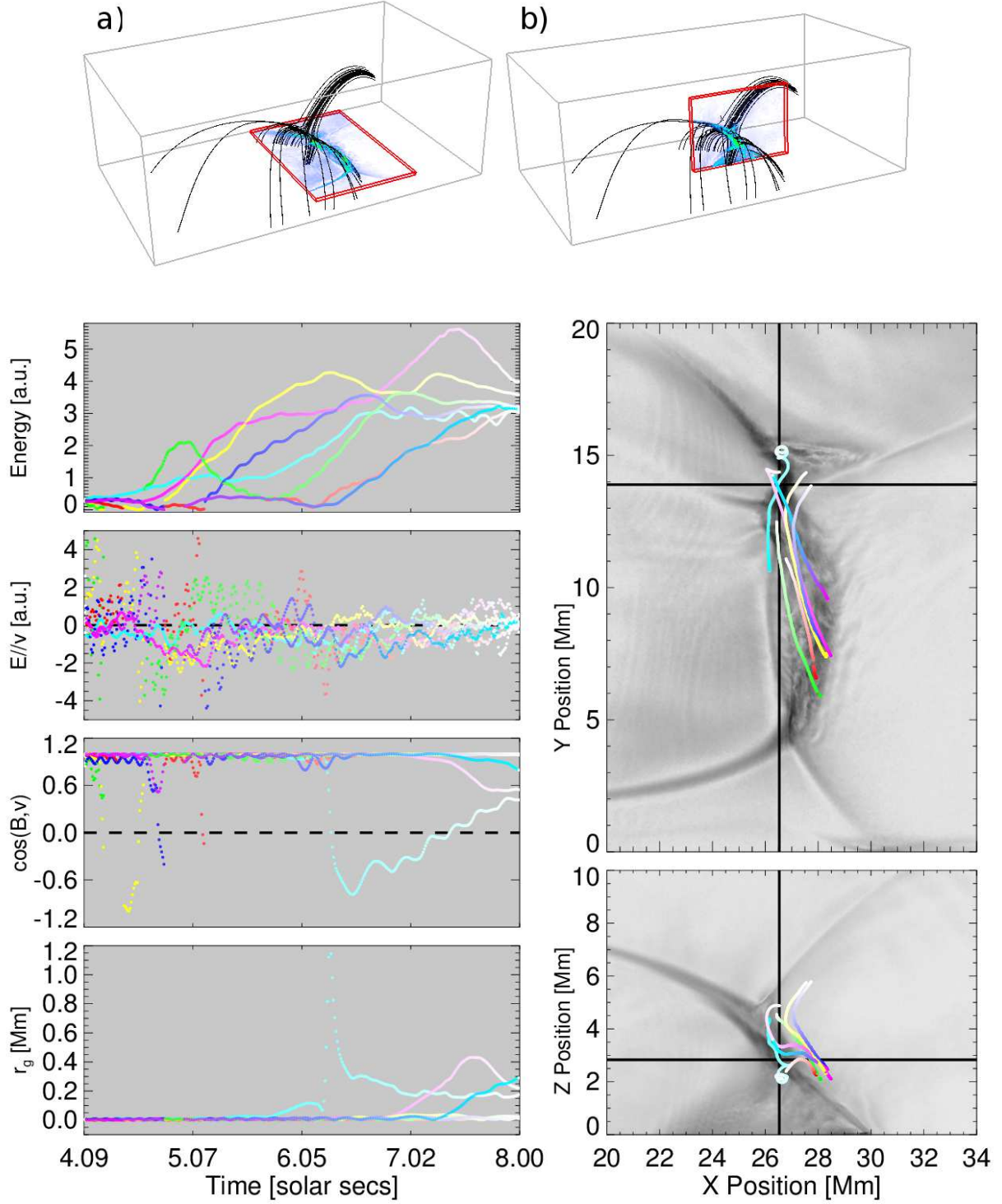


FIG. 4.— Seven randomly chosen accelerated electrons (colored lines) from the power-law energy tail of run 3M. The background gray-scale images to the right are the sum over electric current density slices. See the text for detailed information.

through Ampère's law

$$J = \mu_0^{-1} \nabla \times B \approx \mu_0^{-1} \frac{\Delta B}{\Delta L}, \quad (11)$$

where ΔB is the typical change in the magnetic field across the current sheet and ΔL is the thickness of the current sheet. The current is generated by moving the

electrons

$$J = nvq = n \left(\frac{2Lq^3E}{m_e} \right)^{1/2}, \quad (12)$$

where n is the particle density. Using the above two expressions for J , we obtain an equation for the total

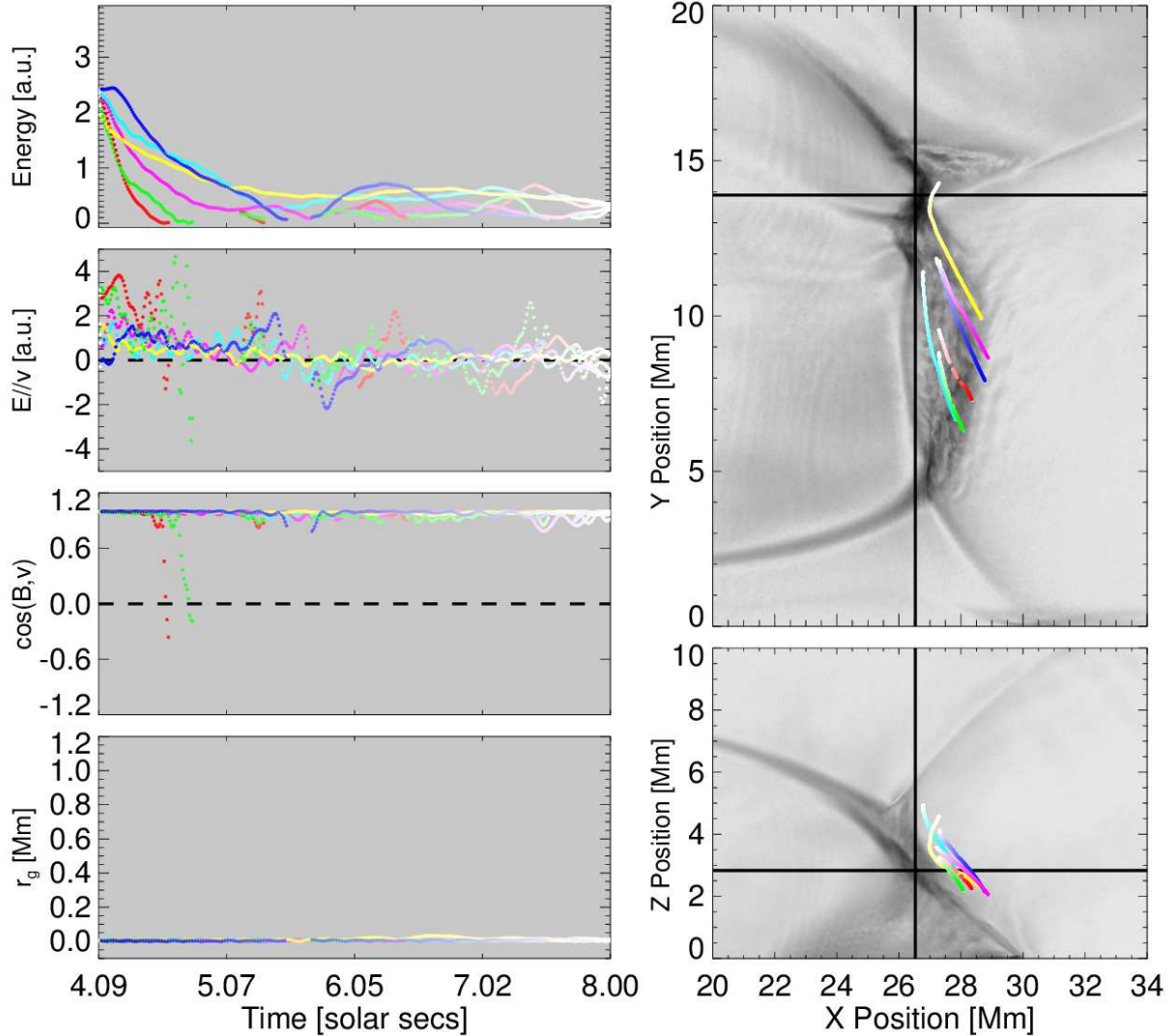


FIG. 5.— Analog to Figure 4, but for randomly chosen electrons from the power-law energy tail of run 3M, which lose energy.

energy gain of a single particle due to the electric field

$$q E L = \mu_0^{-2} \left(\frac{\Delta B}{\Delta L} \right)^2 \frac{m_e}{2n^2 q^2}. \quad (13)$$

Given that this acceleration only happens inside the current sheet the expression can be interpreted as the maximal acceleration a single electron can obtain, if it moves continuously inside the current sheet over the distance L .

To relate Equation (13) to our simulations and real observations, we need the scaling of ΔB and the current sheet thickness ΔL . ΔL is determined by stability constraints, as instabilities diffuse the current away, in case it shrinks below a certain thickness ΔL . There have been several studies in 2D and 2.5D on the current sheet thickness concluding that ΔL is comparable to the size of the diffusion region, as noted in laboratory experiments by Ji et al. (2008), as well as in PIC simulations by Hesse et al. (2001). But these magnetic geometries are not directly comparable to our case, in which most of

the diffusion takes place in the current sheet rather than around an idealized magnetic X-point geometry. In fact, very little is known about the thickness of 3D fan-plane current sheets. We therefore cover here the most probable cases. We assume the smallest length scale over which a coherent large-scale plane of current can be maintained is either the electron gyro-radius r_g in the magnetic field or the electron skin depth:

$$\Delta L \approx \frac{m_e v_{th,e}}{qB} \quad (\text{gyro-radius}) \quad (14)$$

$$\Delta L \approx \left(\frac{m_e}{\mu_0 n q^2} \right)^{1/2} \quad (\text{skin depth}) \quad (15)$$

(if ΔL is instead of the order of the ion gyro-radius it would be larger than the estimate in Equation (14) by a factor $(m_p/m_e)^{1/2}$, which is about a factor of 4 in our case). If we rewrite ΔB as a fractional change in the magnetic field $\Delta B = \epsilon_B B$, and express B and ΔB in

terms of the Alfvén speed v_A in the plasma

$$v_A^2 = \frac{B^2}{\mu_0 n m_p} = \frac{\Delta B^2}{\epsilon_B^2 \mu_0 n m_p} \quad (16)$$

two elegant expressions emerge for Equation (13), defining the maximal electron energy generated by the DC acceleration

$$q E L = \epsilon_B^2 \frac{E_A^2}{E_{th,e}}, \quad (\Delta L \sim \text{gyro-radius}) \quad (17)$$

$$q E L = \epsilon_B^2 E_A, \quad (\Delta L \sim \text{skin depth}) \quad (18)$$

where $E_A = \frac{1}{2} m_p v_A^2$ is the “kinetic Alfvén energy”, which is needed to move information in the system, and $E_{th,e} = \frac{1}{2} m_e v_{th,e}^2$ is the thermal energy of the electrons. If the current sheet thickness is related to the gyro-radius, then the higher the temperature the smaller the acceleration of an individual particle. A higher temperature is also reflected in a larger gyro radius, but the total energy available for acceleration induced by Ampère’s law is the same, and hence there must be more, but lower energy, particles in a thicker current sheet. On the other hand, if the current sheet thickness is related to the electron skin depth the maximum energy should be independent of the temperature. Note that the right-hand side of Equations (17) and (18) only contains macroscopic fluid parameters. Equations (17) and (18) provide an estimate of the electric field and its dependency on the charge per particle; the charge times the electric field magnitude is to lowest order a constant and hence our modifications in charge q_{mod} are reflected in a q_{mod} times too large electric field, where typically $q_{mod} \approx 2 \times 10^6$. Equations similar to 17 or 18 are what we expect to be able to test in the future. As for now the numerical resolution is not sufficient for an experiment to resolve typical gyro radii with enough grid cells, while simultaneously resolving the large-scale plasma.

In the current experiments, the current sheet thickness is essentially determined by the grid spacing, and is generally a few times Δs ; about an order of magnitude larger than the typical electron gyro radii, and about half an order of magnitude larger than the typical proton gyro radii. If, at the same elementary charge per particle q , we were able to increase the numerical resolution in order to resolve the gyro radii and the current sheet became correspondingly thinner, then according to Equation (13) the maximum energy gain would increase with the square of the ΔL factor, so with 1 – 2 orders of magnitude.

We conclude that a conservative estimate of the current sheet electric field in the Sun would be smaller by at most the factor (about 2×10^6) by which the elementary charge per particle has been reduced, and it could possibly be 1 – 2 orders of magnitude larger. Taking 4000 V m^{-1} as a typical magnitude of the electric field in our experiments, we thus come up with a conservative estimate on the order of 2 mV m^{-1} for the solar electric field in a situation analogous to the one we model (which is *not* a flaring situation). Using a less conservative estimate based on the argument of numerical resolution, the electric field is on the order of $20 - 200 \text{ mV m}^{-1}$. In comparison, electric fields *during* solar flares are inferred to be on the order of thousands of V m^{-1} (Qiu et al. 2002).

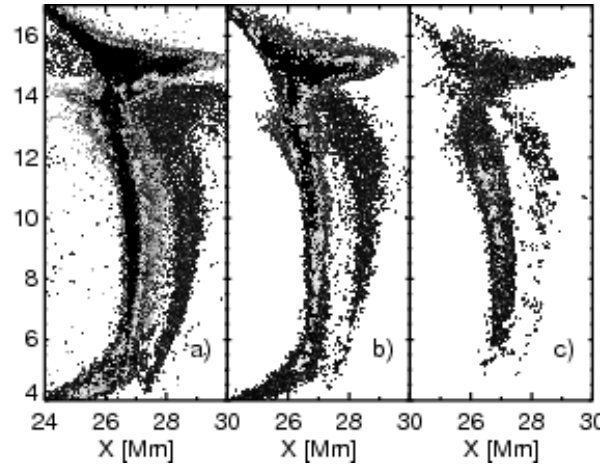


FIG. 6.— Run 5L: power-law tail electric current density (J) contributions from particles within the energy range of (a) $4.3 \times 10^{-22} < e < 1.4 \times 10^{-21}$, (b) $1.4 \times 10^{-21} < e < 4.4 \times 10^{-21}$, and (c) $e > 4.4 \times 10^{-21}$ in (a.u.).

4.3. Magnetic Field Geometry versus Power-law Distribution

As the current sheet channels make up a very small fraction of the domain, most particles will not exhibit the correct angle to exactly pass through an acceleration channel, but will instead be deflected by the magnetic field, ending up outside the current sheet without undergoing a continued acceleration. Hence, most particles are *not* continuously accelerated. The electric current itself is mainly carried by the lowermost part of the power-law distribution, as illustrated in Figure 6, which shows the contributions from the particles to the electric current density from three equally large regions of $\log(\text{energy})$ of the power-law tail of run 5L. The particles of the lowest bin are most probably in constant exchange with the thermal particle distribution. Figure 7 sets the power-law tail in relation to the bulk flow (average velocity of a given species inside a cell) and the thermal particles. The power-law tail dominates over the thermal contribution with respect to contributions to the electric current density. About 0.2% of all electrons in the computational box make up the non-thermal electrons high-energy tail of the distribution. 5% of the total electron energy is carried by the power-law tail particles, while most of this energy is in the most energetic particles of the power-law tail, as illustrated in Figure 8. But, if we only consider particles with a negative vertical velocity, thus moving toward the bottom of the box, and additionally reside in a zone on the lower quarter of the box of $1.9 \times 10^{11} \text{ km}^3$ (from approximately $0.175 - 1.750 \text{ Mm}$ above the bottom boundary), the energy share coming from the power-law tail amounts to over 50% and we find more than 5% of all particles in the high-energy tail population in run 5L, while the total number of electrons in this cut-out is about 1.52×10^7 . These are the particles that on the real sun would be decelerated in the chromosphere, leaving an imprint in the form of observable bremsstrahlung emission.

4.4. Comparison with Observations

Considering the observations of this particular reconnection event, in addition to the bright ribbons observed

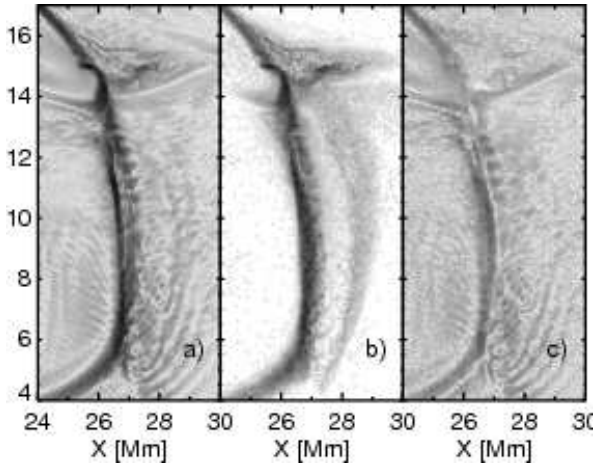


FIG. 7.— Electric current density arising from (a) bulk flow, (b) the power-law tail particles, and (c) the thermal particles in run 5L.

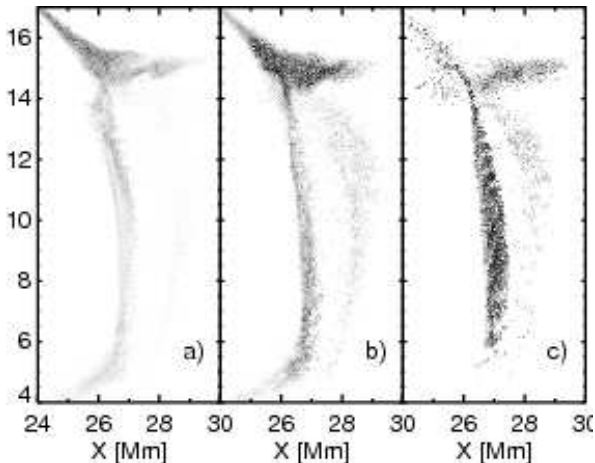


FIG. 8.— Run 5L: power-law tail energy (e) contributions from particles within the energy range of (a) $4.3 \times 10^{-22} < e < 1.4 \times 10^{-21}$, (b) $1.4 \times 10^{-21} < e < 4.4 \times 10^{-21}$, and (c) $e > 4.4 \times 10^{-21}$ in (a.u.).

in $H\alpha$ and UV at the intersection of the fan and the chromosphere (Masson et al. 2009), the chromospheric foot-points of the interchange reconnection region show also soft and hard X-ray signatures during the impulsive phase with a peak intensity slightly northward of the null-point, as shown at the top of Figure 5 in Reid et al. (2012). This coincides well with the impact region of the power-law electrons in our simulation which travel along the fan-plane and finally hit the lower boundary. Figure 9 shows the non-thermal electron energies in the simulation at their impact regions on the lower boundary of the box accumulated over $t = 4 - 9$ seconds. The small difference in the location of the peak intensity compared to observations (Masson et al. 2009; Reid et al. 2012) can at least partly be explained by the driving pattern, which is of course only an approximation to the real photospheric boundary motion. The second reason may be the overall magnetic field at the start of the simulation, which is an outcome of an MHD simulation, which was again initialized from a potential field extrapolation.

However, our electron energies are clearly lower than what is needed for the observed emission spectra to be

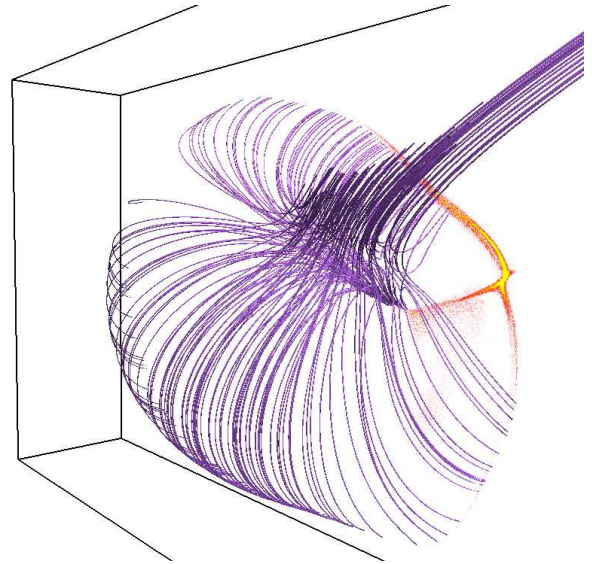


FIG. 9.— Impact area of mainly non-thermal electrons from run 5L. Shown is the electron energy (from orange increasing to yellow) added up at the lower boundary over a period of 5 seconds. Additionally, magnetic field lines (purple) passing close to the null-point are plotted.

produced. Hence, it is important to emphasize that we do not model the observed flare event, but rather the pre-flare phase. One reason is that we use an MHD state taken at a time well before the flare event. Another reason is, as shown in Baumann et al. (2013), that the boundary driver in the MHD simulations, representing the observed horizontal magnetic field motion in the active region, does not provide enough shear and stress to the system to result in an abrupt energy release. Despite that, we expect the qualitative nature of the acceleration mechanism to be the same in the flare phase as in its pre-phase, since the *overall* magnetic morphology during a flaring process does not significantly change, but displays a larger current and hence a larger parallel electric field is required.

4.5. The Energy Distribution and the Influence of the Modifications

Looking at the energy histogram of the same particles considered in Section 4.3; downward moving in a cut-out of the lower part of the simulation box (see top illustration in Figure 10), we find a Maxwell-Boltzmann distribution combined with a $dN/d \ln E = E dN/dE$ power-law index of about -0.78, corresponding to a dN/dE distribution power-law index of -1.78 (see Figure 10). A power-law index of -1.78 implies that the electric current resulting from the power-law population is mainly carried by the low-energy electrons, while the kinetic energy is mainly carried by the highest energy constituents, visualized in Figure 8. The color code in Figure 10 shows the temporal evolution of the energy distribution function for downward-moving particles in the cut-out. The power-law index for the full simulation box is similar. Figure 10 further shows that the tail slope rapidly converges toward the power-law index of about -1.78, indicating an impulsive acceleration of electrons. The weak, apparently non-thermal tail present in the distribution function from the very beginning (black solid line), does not share origin with the power-law tail that is created

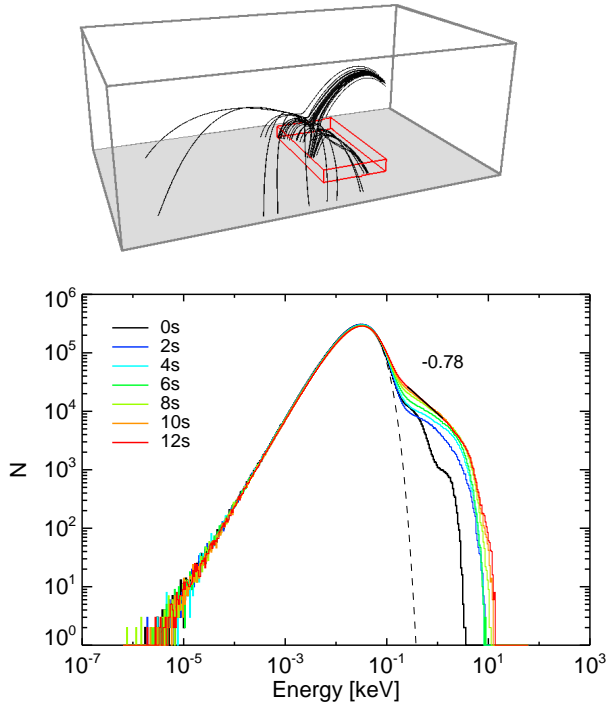


FIG. 10.— Energy distribution of run 5L covering 12 solar seconds from the beginning of the simulation, obtained from 1.52×10^7 electrons in a volume of $1.9 \times 10^{11} \text{ km}^3$ shown in the illustration above the plot. The dashed line represents a Maxwell-Boltzmann distribution fit.

dynamically at later times. It arises due to the electric current in the MHD current sheet (the initial electron velocities are drawn randomly from a Maxwellian distribution, shifted with a systematic velocity to maintain the local electric current density). It is entirely due to the high values of the drift velocity necessitated by our rescaled units, but does not influence the later creation of accelerated particles; they appear also in tests where the electrons are not given a systematic initial velocity.

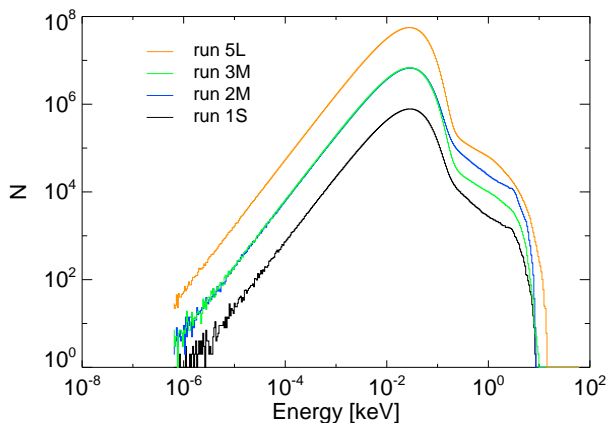


FIG. 11.— Energy histogram for all electrons in the full box for different simulation runs at time $t = 12 \text{ s}$.

A comparison of the different electron energy distributions from the simulation runs listed in Table 1, as previously mentioned in Section 3.2, may be found in Figures 11 and 12. For these plots, all electrons in the

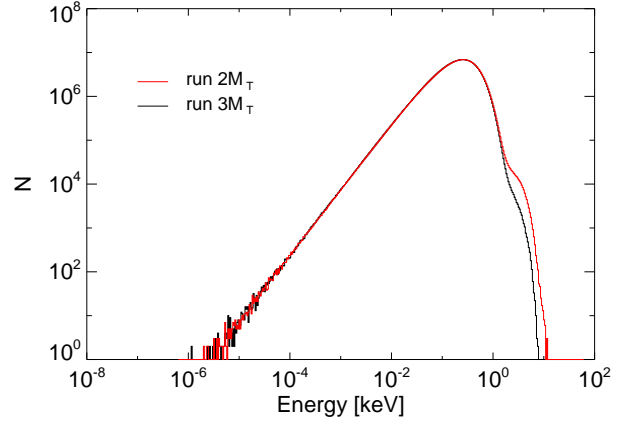


FIG. 12.— Energy histogram for all electrons in the full box at time $t = 12 \text{ s}$ for the simulation runs with double the temperature of the runs presented in Figure 11.

full simulation domain are used. The histograms are not normalized by the number of particles in order to allow for a better power-law index comparison between the different runs. The thermal distribution is the same for all simulations having initially the same temperature profile and it is stable over at least 12 solar seconds, as shown as an example in run 5L (Figure 10). The non-thermal energy tail part quickly approaches a power-law index of about -1.78 for all runs, independently of their resolution. The power law itself is mainly a consequence of the DC systematic electric field particle acceleration and together with the cutoff of the energy histogram presumably a result of the available electric potential difference in the system, which is determined by the current sheet thickness. The thickness, on the other hand, is controlled by the magnetic field geometry and its evolution.

For simulations with initially a higher temperature, see Figure 12, the non-thermal part of the energy distribution drowns in the thermal part. With a plasma beta in the corona $\ll 1$, a change in the temperature is not expected to significantly change the overall electric field (also see Figure 3) and thereby the maximum energy that can be gained by a particle.

Observational support for the power-law index received from our simulations can be found in, e.g., Krucker et al. (2007). There have also been a number of test particle investigations of current sheets, such as Turkmani et al. (2006), Wood & Neukirch (2005) and Zharkova & Gordovskyy (2005) finding similar electron power-law indices — and even slightly harder. But such comparisons are dangerous, as these studies were conducted using the test particle approach and the latter additionally assumed a simplified 3D magnetic and electric field configuration, presumably having a significant influence on the power-law index as partially studied by Zharkova & Gordovskyy (2005).

5. CONCLUSIONS

We presented a first of a kind PIC study of a realistic AR topology. In this study of a pre-flare 3D reconnection region near a 3D magnetic null point in the solar corona, the main electron acceleration mechanism has been shown to be the parallel systematic, almost stationary electric field (‘DC’ electric field), building up as

a consequence of the magnetic reconnection and dissipation close to the null-point and in the fan-plane current sheet of this well-defined magnetic topology. We estimate from the simulation results the average electric field in this quiescent region to be on the order of $20 - 200 \text{ mV m}^{-1}$ in the Sun, which is significantly smaller (2 – 3 orders of magnitude) than what has been found in the corresponding MHD simulations (Baumann et al. 2013). However, this electric field is still sufficient to create a noticeable non-thermal electron power-law tail with power-law indices on the order of what is observed during solar flares (e.g. Krucker et al. 2007). We also present a discussion of the expected dependency of the electric field on the modified elementary charge per particle; showing that the product $E \cdot q$ is expected to be conserved to lowest order. The verification of this relation must be left for future studies due to the current restrictions on computational resources.

The different modification options given in this article serve to reduce the ratio between micro and macro-scales, which is required in order to overcome numerical constraints when simulating realistic physical scales of active regions. The main parameter change used to increase micro-scales is a reduction of the elementary charge per particle, essentially equivalent to a reduction of the particle density. As part of the model validation, we found the electric field values and the non-thermal energy distribution to be only weakly dependent on the applied modifications of the constants of nature. In spite of the modifications of the constants of nature necessary to make this experiment possible we expect that the physical processes in the experiment are qualitatively similar to those in the real Sun, and we therefore see these kinds of studies as a very valuable tool for studying the coupling between kinetic and MHD scales in semirealistic models.

From studies of the locations of the non-thermal electrons and of their acceleration paths we conclude that

the magnetic field geometry and its temporal evolution are likely to be the main factors controlling the power-law index measured in this experiment. We further show that in the lower part of the computational box the electron energy is predominantly in the non-thermal component, with a particle impact area that correlates well with the observations by *TRACE*, *SOHO* and *RHESSI* (Masson et al. 2009; Reid et al. 2012).

In the future, we hope to strengthen our findings with even higher resolution simulations, and we additionally plan to study the temporal dependence of the power-law index by employing longer simulation runs, which would at the same time provide an opportunity to study ion acceleration.

ACKNOWLEDGMENTS

Special thanks go to Jacob Trier Frederiksen and Klaus Galsgaard for very valuable discussions and to Guillaume Aulanier and Sophie Masson for sharing their MHD data with us.

G.B. was supported by the Niels Bohr International Academy and the SOLAIRE Research Training Network of the European Commission (MRTN-CT-2006-035484). T.H. is supported by the Centre for Star and Planet Formation which is financed by the Danish National Science Foundation. The results in this paper have been achieved mainly using the PRACE and John von Neumann Institute for Computing Research Infrastructure resource JUGENE/JUROPA at the Jülich Supercomputing Centre (FZ-J); we thank the center for their assistance. Furthermore we acknowledge use of computing resources at the Danish Center for Scientific Computing in Copenhagen, and at HLRS and FZ-J through the DECI-6 grant SunFlare, as well as funding from the European Commission's Seventh Framework Programme (FP7/2007-2013) under the grant agreement SWIFF (project No. 263340, www.swiff.eu).

REFERENCES

- Aulanier, G., Golub, L., DeLuca, E. E., Cirtain, J. W., Kano, R., Lundquist, L. L., Narukage, N., Sakao, T., & Weber, M. A. 2007, *Science*, 318, 1588
- Bárta, M., Büchner, J., & Karlický, M. 2010, *Advances in Space Research*, 45, 10
- Baumann, G., Galsgaard, K., & Nordlund, Å. 2013, *Sol. Phys.*, 284, 467
- Browning, P. K., Dalla, S., Peters, D., & Smith, J. 2010, *A&A*, 520, A105
- Craig, I. J. D., Fabling, R. B., & Watson, P. G. 1997, *ApJ*, 485, 383
- Dalla, S., & Browning, P. K. 2005, *A&A*, 436, 1103
- . 2008, *A&A*, 491, 289
- Drake, J. F., Swisdak, M., Che, H., & Shay, M. A. 2006, *Nature*, 443, 553
- Esirkepov, T. Z. 2001, *Computer Physics Communications*, 135, 144
- Galsgaard, K., & Pontin, D. I. 2011, *A&A*, 529, A20
- Haugbølle, T. 2005, PhD thesis, Niels Bohr Institute [astro-ph/0510292]
- Haugbølle, T., Trier Frederiksen, J., & Nordlund, A. 2012, *ArXiv Astrophysics e-prints* [astro-ph/1211.4575]
- Hededal, C. 2005, PhD thesis, Niels Bohr Institute [astro-ph/0506559]
- Hesse, M., Birn, J., & Kuznetsova, M. 2001, *J. Geophys. Res.*, 106, 3721
- Isobe, H., Miyagoshi, T., Shibata, K., & Yokoyama, T. 2007, in *Astronomical Society of the Pacific Conference Series*, Vol. 369, *New Solar Physics with Solar-B Mission*, ed. K. Shibata, S. Nagata, & T. Sakurai, 355
- Jess, D. B., Mathioudakis, M., Crockett, P. J., & Keenan, F. P. 2008, *ApJ*, 688, L119
- Ji, H., Ren, Y., Yamada, M., Dorfman, S., Daughton, W., & Gerhardt, S. P. 2008, *Geophys. Res. Lett.*, 35, 13106
- Ko, Y.-K., Raymond, J. C., Lin, J., Lawrence, G., Li, J., & Fludra, A. 2003, *ApJ*, 594, 1068
- Krucker, S., Kontar, E. P., Christe, S., & Lin, R. P. 2007, *ApJ*, 663, L109
- Kumar, P., Cho, K.-S., Bong, S.-C., Park, S.-H., & Kim, Y. H. 2012, *ApJ*, 746, 67
- Liu, W. J., Chen, P. F., Ding, M. D., & Fang, C. 2009, *ApJ*, 690, 1633
- Longcope, D. W., McKenzie, D. E., Cirtain, J., & Scott, J. 2005, *ApJ*, 630, 596
- Masson, S., Pariat, E., Aulanier, G., & Schrijver, C. J. 2009, *ApJ*, 700, 559
- Miller, J. A., Cargill, P. J., Emslie, A. G., Holman, G. D., Dennis, B. R., LaRosa, T. N., Winglee, R. M., Benka, S. G., & Tsuneta, S. 1997, *J. Geophys. Res.*, 102, 14631
- Miller, J. A., Larosa, T. N., & Moore, R. L. 1996, *ApJ*, 461, 445
- Milligan, R. O., Gallagher, P. T., Mathioudakis, M., Bloomfield, D. S., Keenan, F. P., & Schwartz, R. A. 2006, *ApJ*, 638, L117
- Nordlund, A., & Galsgaard, K. 1997, A 3D MHD code for Parallel Computers, Tech. rep., Niels Bohr Institute
- Petrosian, V., Yan, H., & Lazarian, A. 2006, *ApJ*, 644, 603
- Priest, E. R., & Schrijver, C. J. 1999, *Sol. Phys.*, 190, 1
- Priest, E. R., & Titov, V. S. 1996, *Royal Society of London Proceedings Series A*, 354, 2951
- Qiu, J., Lee, J., Gary, D. E., & Wang, H. 2002, *ApJ*, 565, 1335
- Reid, H. A. S., Vilmer, N., Aulanier, G., & Pariat, E. 2012, *A&A*, 547, A52
- Rosdahl, K. J., & Galsgaard, K. 2010, *A&A*, 511, A73
- Siversky, T. V., & Zharkova, V. V. 2009, *Journal of Plasma Physics*, 75, 619

- Sugiyama, T., & Kusano, K. 2007, *Journal of Computational Physics*, 227, 1340
- Sui, L., Holman, G. D., & Dennis, B. R. 2004, *ApJ*, 612, 546
- Toriumi, S., & Yokoyama, T. 2012, *A&A*, 539, A22
- Turkmani, R., Cargill, P. J., Galsgaard, K., Vlahos, L., & Isliker, H. 2006, *A&A*, 449, 749
- Turkmani, R., Vlahos, L., Galsgaard, K., Cargill, P. J., & Isliker, H. 2005, *ApJ*, 620, L59
- Vay, J.-L. 2008, *Physics of Plasmas*, 15, 056701
- Vlahos, L., Isliker, H., & Lepreti, F. 2004, *ApJ*, 608, 540
- Wood, P., & Neukirch, T. 2005, *Sol. Phys.*, 226, 73
- Yee, K. 1966, *IEEE Transactions on Antennas and Propagation*, 14, 302
- Zharkova, V. V., & Gordovskyy, M. 2005, *Space Sci. Rev.*, 121, 165